ACS APPLIED MATERIALS & INTERFACES

www.acsami.org

Research Article

Photoswitchable Antioxidant and Prooxidant Activities of Mg-Doped Carbon Dot Nanozymes as Antibacterial and Anti-Inflammatory Agents

Published as part of ACS Applied Materials & Interfaces special issue "Nanozymes: Design, Mechanisms, and Applications."

Jinyu Shi,[#] Yu Zhang,[#] Xiangyang Fang, Xing Fan, Jing Li, Chuan-Hua Zhou,* Zhining Xia,* Dai-Wen Pang,* and Cui Liu*

Cite This: *ACS Appl. Mater. Interfaces* 2025, 17, 26467−26479

Read Online

ACCESS | Metrics & More | Article Recommendations | Supporting Information

ABSTRACT: Multienzymatic nanozymes hold great potential in therapeutics due to their higher catalytic efficiency and multifunctionality. However, flexibly switching the antioxidant and prooxidant activities of multienzymic nanozymes at the same lesion remains a challenge. Herein, we design magnesium-doped carbon dot (Mg-CD) nanozymes with photoswitchable antioxidant and prooxidant activities under physiological conditions. The Mg-CD nanozymes exhibit superoxide dismutase (SOD)-like activity and can scavenge singlet oxygen and hydroxyl radicals without illumination. Interestingly, the antioxidant activity can be converted to oxidase-like activity under visible light illumination, producing singlet oxygen and superoxide anions. The mechanism of the switchable activities is attributed to the fact that coordination between magnesium and the CD skeleton enhances the excited-state electron transfer of singlet states and the energy transfer of triplet electrons. Therefore, Mg-CDs can act as antibacterial and anti-inflammatory agents. Mg-CDs exhibit antibacterial rates exceeding 99% within 5 min under illumination. They can scavenge reactive oxygen species, thereby showing excellent capacity in treating inflammatory wounds caused by lipopolysaccharide. These photoswitchable antioxidant and prooxidant activities of CD nanozymes offer an effective strategy for better manipulating the versatility of nanozymes, expanding their intelligent biomedical applications.

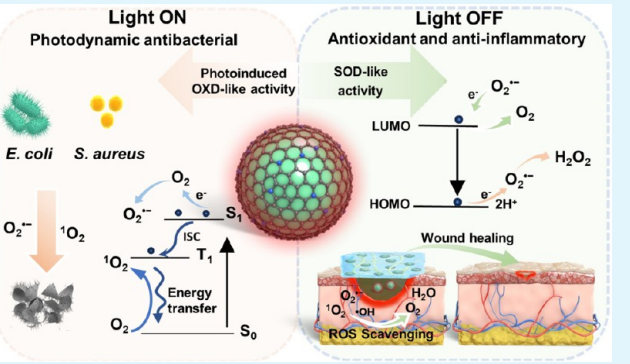

KEYWORDS: *carbon dots, nanozymes, antibacterial, photoswitchable, anti-inflammatory*

1. INTRODUCTION

Nanozymes have been widely used in biomedicine due to their advantages such as low cost, high stability, and easy operation.[1−6] Since the first report of peroxidase (POD)-like activity of Fe_3O_4 nanoparticles in 2007,[7] various nanomaterials exhibiting enzyme-like activities have been successively reported, such as noble metals,[8] metal oxides,[9] and carbon nanomaterials.[10] Their catalytic types cover oxidoreductases, hydrolases, lyases, and isomerases.[3] Among these, carbon-based nanozymes show great potential in the biomedical field due to their low cost, high catalytic activity, and good biocompatibility.[11] Nanozymes with more than one kind of enzyme-like activity are termed multienzymatic nanozymes, which have received increasing attention in recent years due to their multifunctionality and have great application potential in fields such as biosensing and therapy. Compared with nanozymes with single enzyme-like activity, multienzymatic nanozymes usually exhibit higher catalytic efficiency due to synergistic and cascade effects.[12] For example, Au nanozymes exhibited pH-switchable peroxidase (POD) and catalase (CAT) activities.[13] Prussian blue nanozymes have POD, CAT, and superoxide dismutase (SOD)-like activities.[14,15] The oxidase (OXD) or POD-like activities can catalyze oxygen or hydrogen peroxide to generate reactive oxygen species (ROS), which can be used for antibacterial,[16] antitumor,[17] and sensing.[13] The CAT-like activity can catalyze endogenous hydrogen peroxide to generate oxygen to relieve hypoxia in the tumor site and thus solve the poor efficacy of tumor photodynamic, radiation, and sonodynamic therapies caused

Received: March 11, 2025
Revised: April 16, 2025
Accepted: April 17, 2025
Published: April 28, 2025

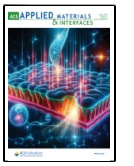

Scheme 1. Synthesis of Mg-CDs and their Antibacterial and Anti-Inflammatory- Applications

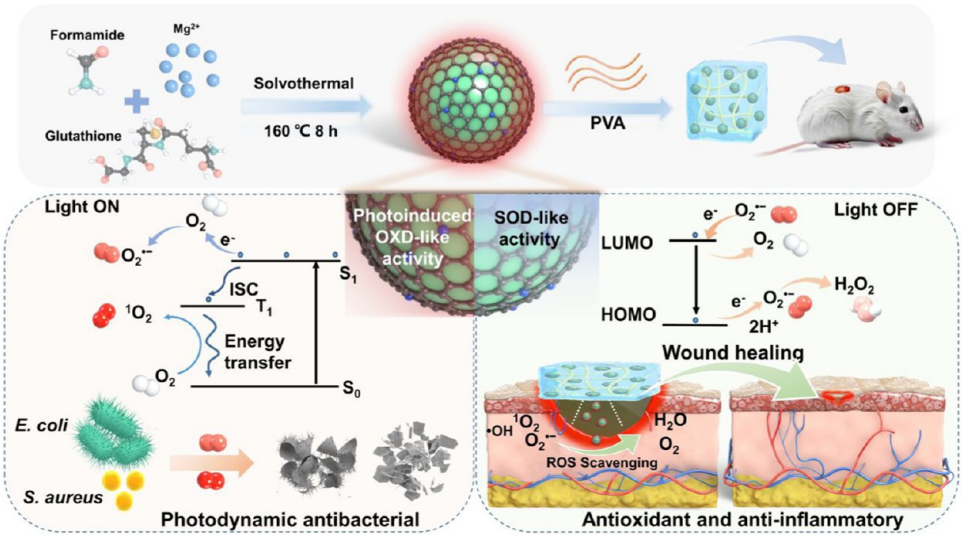

by insufficient endogenous oxygen. Nanozymes with SOD-like activity can catalyze the decomposition of ROS into oxygen or water, alleviating the adverse oxidative stress of cells and tissues, and are used for antioxidant treatment of various diseases such as stroke, acute and chronic inflammation, and cardiovascular and cerebrovascular diseases.[18−20] However, how to balance the opposite enzyme-mimicking activities and eliminate the interference brought about by multifunctional properties is of great importance for the practical application of multienzymic nanozymes.

Generally, under acidic conditions, pro-oxidative catalytic activity dominates, while under alkaline conditions, antioxidant catalytic activity prevails. Therefore, pH has been an effective way to regulate the activities of multienzymatic nanozymes. However, this is very inconvenient in practical biomedical applications. For example, for a certain lesion, its pH is difficult to change drastically with the occurrence and development of the disease. Therefore, it is of great significance to develop more effective switching methods to achieve the synergy application of antioxidant and prooxidant activities of nanozymes. Light also plays an important role in the catalytic process of natural enzymes.[21,22] For example, DNA photolyase,[23] fatty acid photodecarboxylase,[24] and protochlorophyllide oxidoreductase[25,26] are all light-activated enzymes. In this regard, photoactivated nanozymes that can absorb light and have photoregulated catalytic activity have been developed. For example, He et al.[27] synthesized carbon dots (CDs) with OXD-like and SOD-like activities. The CDs exhibit photoactivated OXD-like activity at pH 5.0, which can catalyze O_2 into ROS. Besides, they show SOD-like activity under neutral and slightly alkaline conditions. Based on the different catalytic activities of CDs under various pH values, they were applied to promote the healing of bacteria-infected wounds. However, there are few reports on switching the antioxidant and prooxidant catalytic activities of nanozymes through light irradiation under physiological conditions.

Previous works have shown that the doping of metal ions could enhance the catalytic activity of CDs by modifying their bandgap and promoting electron transfer.[28−30] It is widely acknowledged that Mg^{2+} plays an important role in photosynthesis.[31] Our latest work[32] demonstrated that Mg doping could enhance the photoinduced OXD-like activity of CDs. Herein, the photoswitchable catalytic activity of magnesium-doped CD (Mg-CD) nanozymes was investigated. The Mg-CDs show photoinduced OXD-like activity under illumination at a natural pH. They can catalyze O_2 into superoxide anion ($O_2^{\bullet-}$) and singlet oxygen ($^1O_2$). Besides, they exhibit SOD-like activity and can scavenge $^1O_2$ and $^{\bullet}OH$ without illumination. The conversion of multienzyme activities is attributed to the fact that the coordination between magnesium and the CD skeleton enhances the excited-state electron transfer of singlet states and the energy transfer of triplet electrons. Based on the remarkable photoswitch of "ROS-producing" and "ROS-scavenging," Mg-CDs could be used in antibacterial and anti-inflammatory therapies (Scheme 1). The antibacterial results *in vitro* indicate that Mg-CDs can kill most Gram-negative bacteria (taking *Escherichia coli* (*E. coli*) as an example) and Gram-positive bacteria (taking *Staphylococcus aureus* (*S. aureus*) as an example) within 5 min under illumination with antibacterial rates of more than 99%. Besides, Mg-CDs can eliminate biofilms *in vitro*, further addressing the issue of biofilm accumulation caused by bacterial infections. By combining with poly(vinyl alcohol) (PVA), we designed a PVA/Mg-CDs hydrogel dressing through physical cross-linking (Scheme 1), which successfully promoted the healing of acute inflammatory wounds. The photoswitchable multienzymatic activities of Mg-CDs provide a strategy for switching the antioxidant and prooxidant catalytic activities of CD nanozymes, boosting the intelligent biomedical applications of multienzymic nanozymes.

2. RESULTS AND DISCUSSION

The Mg-doped CDs were synthesized by a one-step solvothermal method using $MgCl_2{\cdot}6H_2O$, glutathione (reduced), and formamide as raw materials, based on our previous work.[33] We prepared a series of Mg-CDs with different doping amounts of Mg(II) by tuning the dose of $MgCl_2{\cdot}6H_2O$ in the synthesis process. The samples prepared with the $MgCl_2{\cdot}6H_2O$ dose of 2.5, 5, 10, 20, 40, and 80 mg were denoted as Mg2.5-CDs, Mg5-CDs, Mg10-CDs, Mg20-CDs, Mg40-CDs, and Mg80-CDs, respectively.

The ICP-MS results showed that the doping amounts of Mg(II) in Mg2.5-CDs, Mg5-CDs, Mg10-CDs, Mg20-CDs, Mg40-CDs, and Mg80-CDs were 0.500, 1.010, 1.890, 4.080,

https://doi.org/10.1021/acsami.5c05025
ACS Appl. Mater. Interfaces 2025, 17, 26467−26479

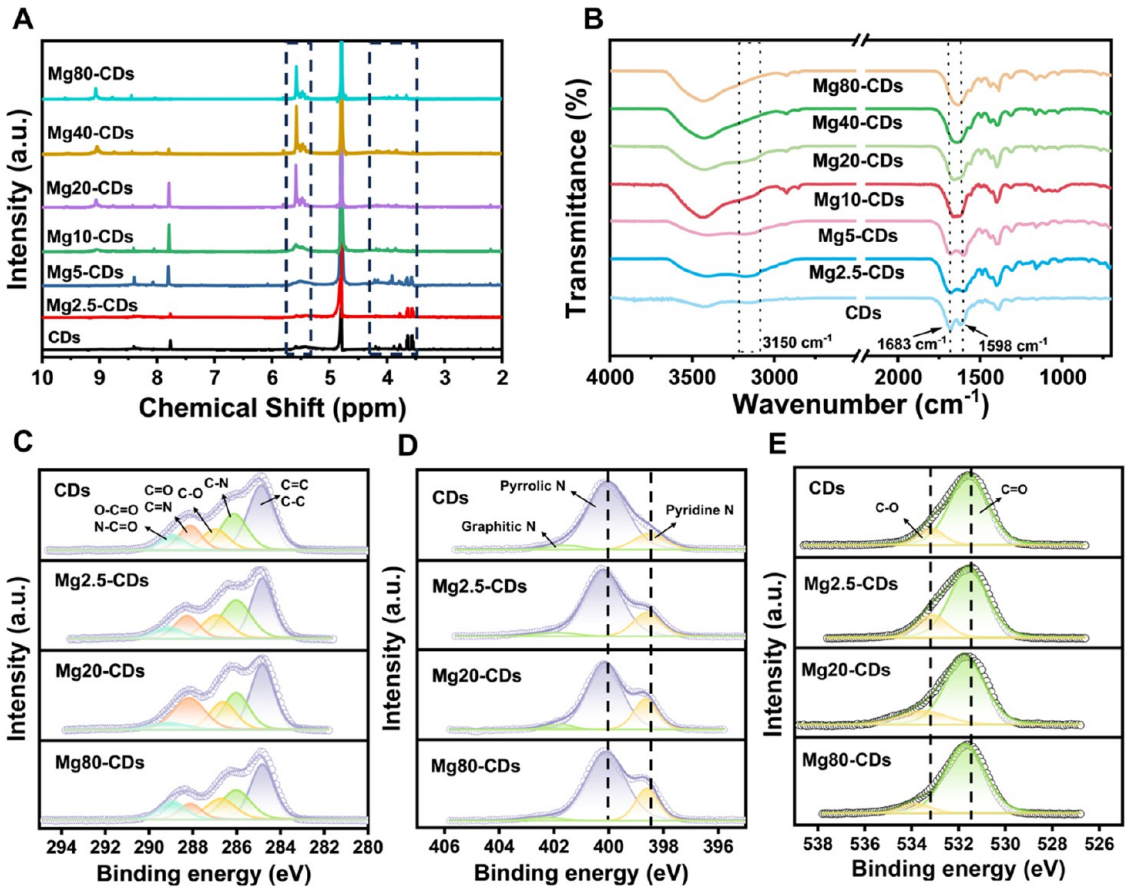

Figure 1. Structure characterizations of Mg-CDs. The (A) ^{1}H NMR and (B) FT-IR spectra of CDs without metal doping, Mg2.5-CDs, Mg5-CDs, Mg10-CDs, Mg20-CDs, Mg40-CDs, and Mg80-CDs, the high-resolution (C) C 1s, (D) N 1s, and (E) O 1s spectra of CDs, Mg2.5-CDs, Mg20-CDs, and Mg80-CDs.

4.576, and 4.994%, respectively (Table S1). Proton magnetic resonance spectroscopy (^{1}H NMR) was used to characterize the structures of these Mg-CDs. As shown in Figure 1A, the peaks ranging from 3.5 to 4.2 ppm were assigned to the α-H of carbonyl and hydroxyl groups. The peak near 5.5 ppm was attributed to the H of alkene, and the peak at ~7.8 ppm was attributed to the H of aromatic rings.[34] Compared to the ^{1}H NMR spectrum of CDs without metal doping, the intensities of peaks near 5.5 ppm increased, and the intensities of peaks ranging from 3.5 to 4.2 ppm decreased. Our latest work showed that there was an interconversion between enol and ketone in the structure of CDs.[35] Therefore, we speculated that Mg^{2+} might coordinate with the hydroxyl groups of enols in CDs, which promotes the transformation of ketone to enol. Figure 1B shows the Fourier transform infrared (FT-IR) spectra of a series of Mg-CDs. Similar to CDs, there were abundant functional groups on the surface of Mg-CDs. The characteristic peaks at 1683 and 1598 cm^{-1} were ascribed to the stretching vibration of C═O in amide and the stretching vibration of C═C, respectively. The characteristic peak at 1401 cm^{-1} was assigned to the stretching vibration of C−N, while that at 3150 cm^{-1} could be attributed to the stretching vibration of N−H.[36] Compared to the FT-IR spectrum of CDs, the intensity of these characteristic peaks of N−H and amide decreased with an increasing doping amount of Mg^{2+}. Based on the above results, it can be speculated that Mg(II) coordinated with N and O atoms in the skeleton of CDs.

In order to further investigate the coordination of Mg(II) and CDs, X-ray photoelectron spectroscopy (XPS) was used to characterize the structures of CDs without Mg(II), and Mg-CDs with low, medium, and high doping amounts of Mg(II). As shown in Figure S1, the XPS survey spectra of CDs, Mg2.5-CDs, Mg20-CDs, and Mg80-CDs displayed four peaks at 169, 285, 400, and 531 eV, which corresponded to S 2p, C 1s, N 1s, and O 1s, respectively.[33] Besides, an obvious peak at 1303 eV corresponding to the Mg 1s appeared in the XPS spectra of Mg2.5-CDs, Mg20-CDs, and Mg80-CDs. The peak intensity increased with increasing doping amounts of Mg(II). In the high-resolution XPS spectra of C 1s (Figure 1C) of these samples, there were five peaks at 284.8, 286.1, 286.9, 288.1, and 288.9 eV attributed to the C═C/C−C, C−N, C−O, C═O/C═N, and O−C═O/N−C═O, respectively. Figure 1D shows the high-resolution N 1s XPS spectra of CDs, Mg2.5-CDs, Mg20-CDs, and Mg80-CDs. In the spectrum of CDs, there were three peaks at 401.5 eV, 400.1, and 398.5 eV, which corresponded to graphitic N, pyrrolic-like N, and pyridine N,[33,36,37] respectively. After doping Mg(II), the binding energy of pyrrolic-like N and pyridine N shifted to 400.2 and 398.6 eV, respectively. The content of pyridine N in CDs was 15.44%, and it increased to 20.49, 20.72, and 22.75% when the dosage of $MgCl_2{\cdot}6H_2O$ was 2.5, 20, and 80 mg, respectively. This may be due to the coordination of Mg(II) with the N atom. In the high-resolution XPS spectra of the polarized O 1s (Figure 1E), there are two peaks at 531.5 and 533.1 eV, which correspond to C═O and C−O. The binding energy of C═O

https://doi.org/10.1021/acsami.5c05025
ACS Appl. Mater. Interfaces 2025, 17, 26467−26479

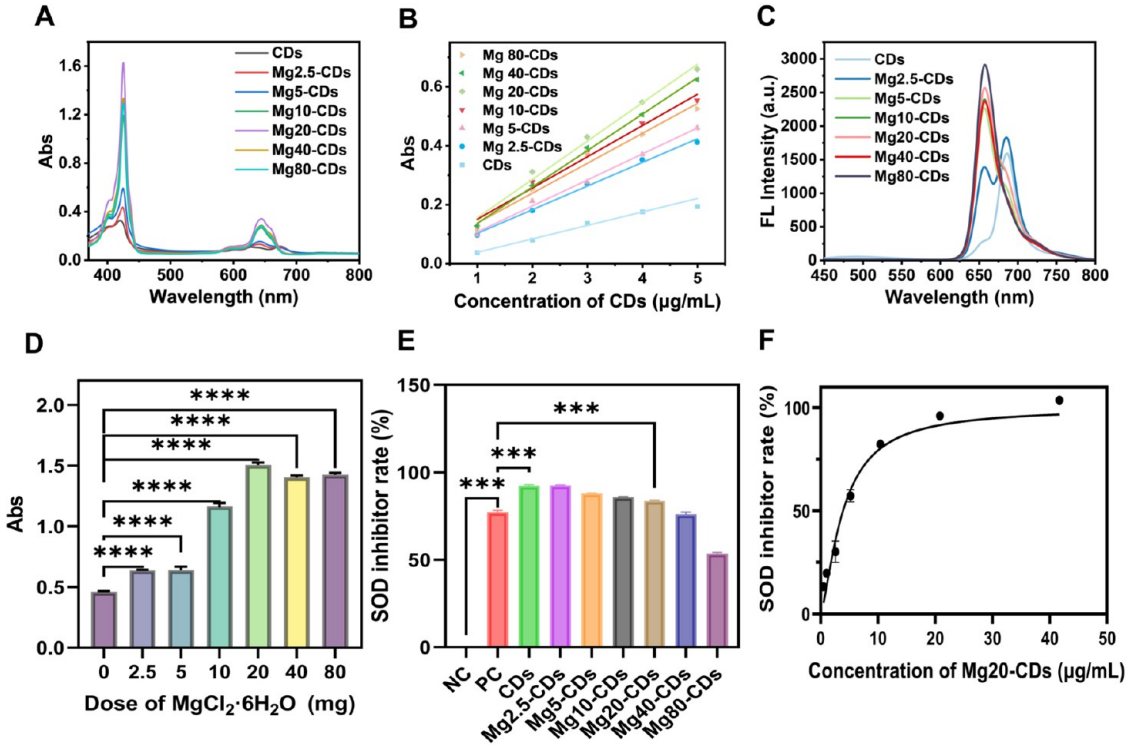

Figure 2. (A) UV−vis absorption spectra of CDs, Mg2.5-CDs, Mg5-CDs, Mg10-CDs, Mg20-CDs, Mg40-CDs, and Mg80-CDs; (B) relationship between the concentration of different CDs and their absorbance at 425 nm; (C) fluorescence spectra; (D) photoinduced OXD-like activity; (E) SOD inhibitor rates of CDs, Mg2.5-CDs, Mg5-CDs, Mg10-CDs, Mg20-CDs, Mg40-CDs, and Mg80-CDs; and (F) SOD-like activity of Mg20-CDs. For (E), NC: negative control (buffer), PC: positive control (natural SOD, 50,000 U/g, final concentration of 20.83 μg/mL), the final concentration of CDs and Mg-CDs was 10.42 μg/mL. In panels D and E, data are presented as means ± SD from three independent experiments. Statistical comparisons were analyzed by One-way ANOVA Tukey's multiple comparison test. *p < 0.05, **p < 0.01, ***p < 0.001, ****p < 0.0001, and n. s., not significant.

and C−O shifted to 531.7 and 533.5 eV after doping Mg(II). It may be due to the doping of Mg(II) changing the electron cloud intensity of O atom.

Then, the optical properties of the Mg-CDs were investigated. Figure 2A shows the UV−vis absorption spectra of CDs, Mg2.5-CDs, Mg5-CDs, Mg10-CDs, Mg20-CDs, Mg40-CDs, and Mg80-CDs. There were several obvious absorption peaks in the ranges of 380−450 and 630−680 nm, which correspond to the $\pi-\pi^*$ and $n-\pi^*$ transitions of C═C and C═N of the π-system.[36,37] It is obvious that the absorbance of Mg-CDs increased and then decreased with the Mg(II) doping amount. The Mg20-CDs had the maximum absorbance. Additionally, the absorption coefficients of these Mg-CDs at an optimal absorption wavelength of 425 nm were calculated (Figures 2B and S2). The results demonstrated that Mg doping significantly enhanced the extinction coefficient of CDs (Table S2). The highest extinction coefficient appeared in Mg20-CDs (0.13013 cm^{-1} μg^{-1} mL), which was more than 3 times that of the CDs without Mg doping. It can be speculated that the coordination between Mg(II) and the CD skeleton could enhance the rigidity of the π-system of CDs and promote electron transitions.

The fluorescence spectra of these CDs are shown in Figure 2C. The fluorescence spectrum of CDs exhibited a strong emission peak at 686 nm and a shoulder peak at 658 nm under an excitation wavelength of 420 nm. After doping with Mg(II), the emission peak at 686 nm decreased, while that at 658 nm increased significantly with the increase in the doping amount of Mg(II). When the dose of $MgCl_2·6H_2O$ in the synthesis process exceeded 5 mg, the fluorescence intensity did not change significantly. There is a transformation between enol and keto in CDs, and the emission peaks at 658 and 686 nm are ascribed to enol and keto forms, respectively.[35] As mentioned above, the results of ^{1}H NMR indicated that the alkene content increased with an increasing doping amount of Mg(II). So, we have reason to believe that Mg(II) preferentially coordinated with the enol structure in CDs, facilitating the transfer from keto to enol and therefore boosting the emission at 658 nm. Furthermore, the absolute quantum yields (QYs) of these CDs were measured (Table S3), showing that doping with Mg(II) enhanced the QY of the CDs. As shown in Table S4, the lifetime of CDs was 4.85 ns, and the lifetime shortened with the increasing doping amount of Mg. This result illustrated that the coordination between Mg(II) and the CD skeleton could reduce the proportion of nonradiative transitions by improving the rigidity of the CD structure, thereby enhancing the fluorescence property of the CDs. The enhanced QY and absorbance capacity allow Mg-CDs to have a higher fluorescence brightness than CDs and exhibit great potential for *in vivo* imaging.

The catalytic activities of these CDs were tested using 3,3′,5,5′ -tetramethyl benzidine (TMB) hydrochloride as a substrate. As shown in Figure S3, only when both O_2 and the light were present could the absorption peaks of ox-TMB (at 370 and 652 nm) be observed. It may be because of the fact that O_2 can be catalyzed by Mg20-CDs under irradiation to produce ROS, thereby oxidizing TMB to ox-TMB. This indicates that Mg20-CDs exhibit photoinduced OXD-like

https://doi.org/10.1021/acsami.5c05025
ACS Appl. Mater. Interfaces 2025, 17, 26467−26479

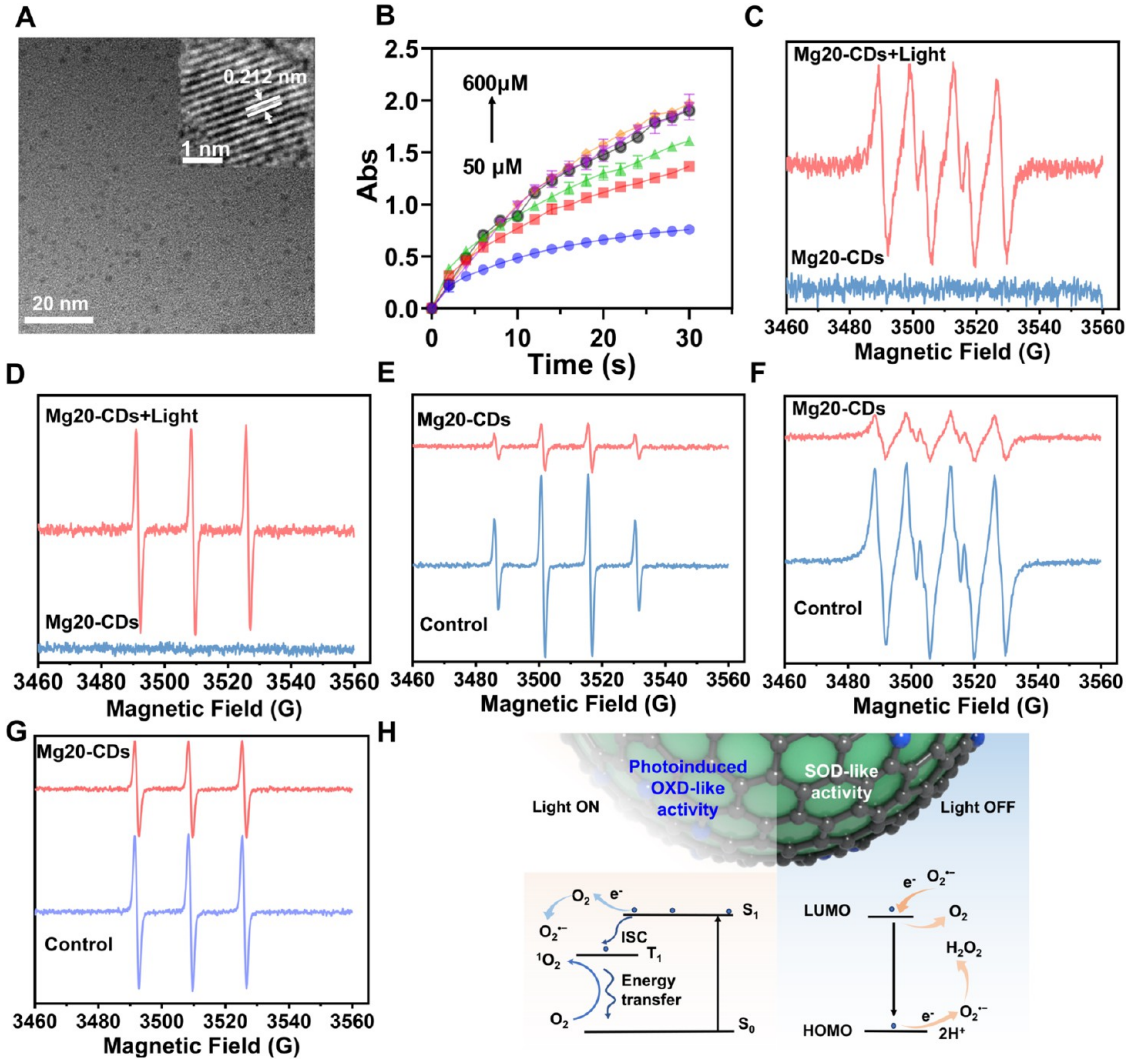

Figure 3. (A) TEM image of Mg20-CDs (inset: high-resolution TEM image), (B) catalytic kinetics of Mg20-CDs toward TMB, and (C) $O_2^{\bullet-}$ and (D) $^1O_2$ producing activities of Mg20-CDs with illumination. (E) $^{\bullet}OH$, (F) $O_2^{\bullet-}$, and (G) $^1O_2$ scavenging activities of Mg20-CDs without illumination. (H) Schematic illustration of the photoswitchable antioxidant and prooxidant catalytic processes of Mg-CDs.

activity. We found that the Mg-CDs exhibited an enhanced photoinduced OXD-like activity under illumination, compared with CDs. As shown in Figure 2D, the doping of Mg(II) enhanced the photoinduced OXD-like activity of CDs significantly, and this activity increased with the amount of $MgCl_2{\cdot}6H_2O$. The absorbance of ox-TMB reached a plateau when the amount of $MgCl_2{\cdot}6H_2O$ was 20 mg. The photoinduced OXD-like activity of Mg20-CDs was about 3 times higher than that of CDs without Mg(II) doping.

Moreover, the SOD-like activities of these CDs were investigated using a superoxide dismutase assay kit. As shown in Figure 2E, the SOD inhibition rate slightly decreased with the increasing contents of Mg(II). It is evident that the doping of Mg(II) significantly improved the fluorescence property and photoinduced OXD-like activity of CDs, but it slightly reduced the SOD-like activity. However, the SOD-like activity of Mg20-CDs was compared with that of natural SOD, and the results showed that the inhibition rate of Mg20-CDs (at a concentration of 10.42 μg/mL) was higher than that of natural SOD (20.83 μg/mL, 50,000 U/g, from SHENZHEN SIYOMICRO BIO-TECH CO LTD). The SOD-like activity of Mg20-CDs was quantitatively determined to be >1000 U/mg (Figure 2F). Taking the above properties into consideration, we selected Mg20-CDs for subsequent research.

Transmission electron microscopy (TEM) was used to characterize the morphology of Mg20-CDs. As shown in Figure 3A, Mg20-CDs exhibited uniform distribution, with an average particle size of 2.1 ± 0.5 nm (Figure S4), which was similar to that of CDs (2.7 ± 0.5 nm, Figure S5A–B). The lattice spacing of 0.21 nm corresponds to the (100) plane of graphite.[38] Besides, the morphology of Mg20-CDs after irradiation was also characterized. As shown in Figure S5C–D, there were no obvious changes in the morphology and particle size of Mg20-CDs after illumination, indicating that the illumination had no impact on the morphology of the Mg20-CDs. The photoinduced OXD-like activity kinetics of Mg20-CDs were further investigated by using TMB as a substrate (Figure 3B). According to the Michaelis–Menten equation, the K_m value of Mg20-CDs was calculated to be 122.3 μM (Figure S6), showing a stronger affinity for TMB compared to other CDs with photoinduced OXD-like activity (Table S5). The stability of Mg20-CDs was investigated, too. As shown in Figure S7, there were no obvious changes in the UV–vis absorption spectra and fluorescence spectra of Mg20-

https://doi.org/10.1021/acsami.5c05025
ACS Appl. Mater. Interfaces 2025, 17, 26467–26479

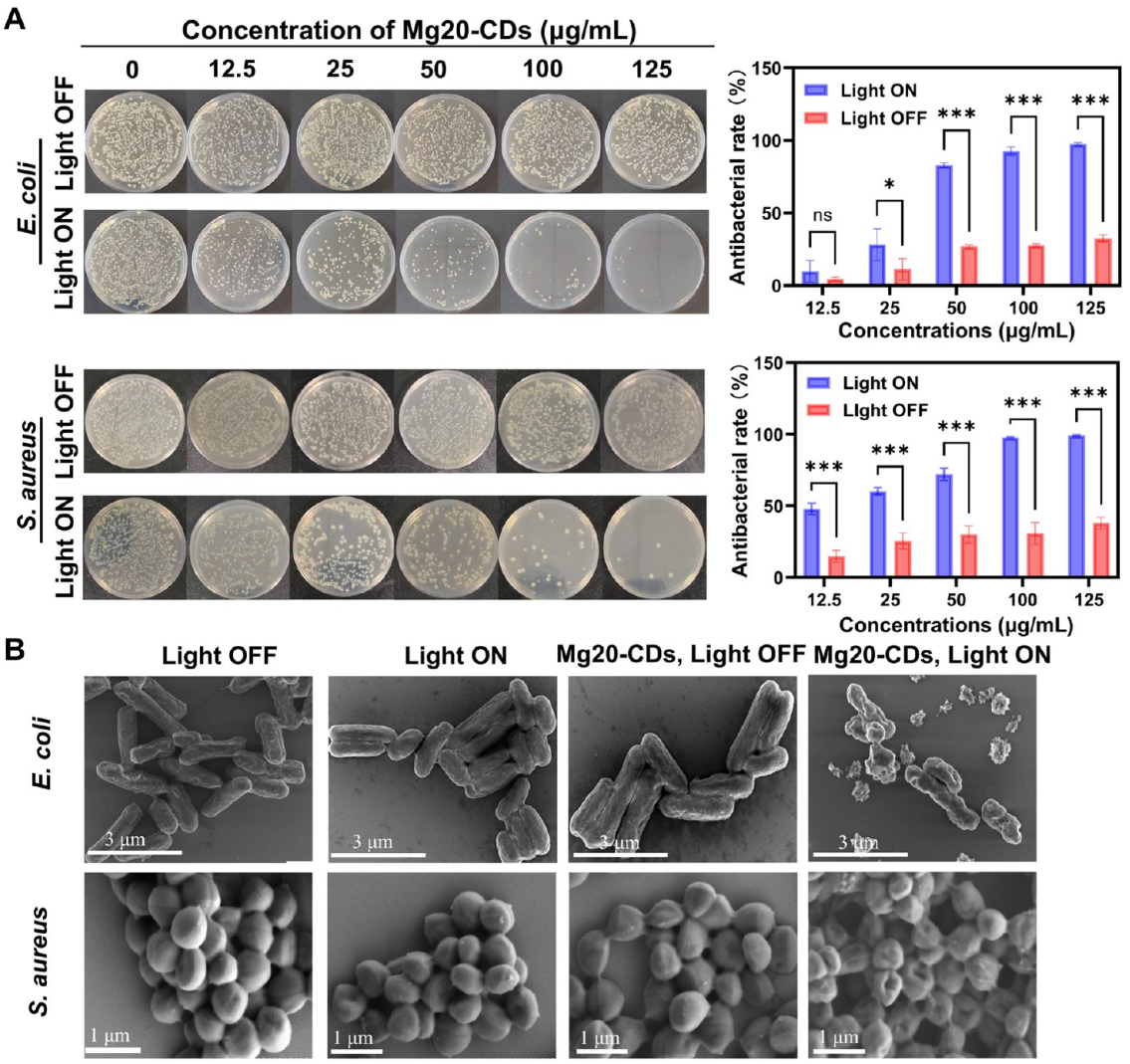

Figure 4. Antibacterial Characteristics of Mg20-CDs. (A) Colonies of *E. coli* and *S. aureus* treated with Mg20-CDs at different concentrations with and without illumination and (B) SEM images of *E. coli* and *S. aureus* treated with Mg20-CDs with and without illumination. In panel A, data are presented as means ± SD from three independent experiments. Statistical comparisons were analyzed by Two-way ANOVA Tukey's multiple comparison test. *$p < 0.05$, **$p < 0.01$, ***$p < 0.001$, ****$p < 0.0001$, and n. s., not significant.

CDs after being stored for 0 and 150 days. Moreover, the photoinduced OXD-like activity also remained basically unchanged. These results indicated the good stability of Mg20-CDs.

Electron spin resonance (EPR) spectroscopy was used to confirm the type of ROS produced under illumination by Mg20-CDs. 5,5-Dimethyl-1-pyrroline N-oxide (DMPO) was used as the trapping agent for $^{\bullet}OH$ and $O_2^{\bullet-}$, while 2,2,6,6-tetramethyl-1-piperidine (TEMP) was used to trap $^1O_2$. As shown in Figure 3C,D, compared to the signals of the mixture of the trapping agent and Mg20-CDs without illumination, the characteristic signals of DMPO/$O_2^{\bullet-}$ and TEMP/$^1O_2$ were clearly observed under illumination. However, there was no significant signal of DMPO/$^{\bullet}OH$ observed (Figure S8). This suggests that Mg20-CDs catalyze O_2 to produce $O_2^{\bullet-}$ and $^1O_2$ under illumination. In order to verify the scavenging capability of Mg20-CDs for each ROS, the Fenton reaction was used to generate ·OH and xanthine oxidase was used to catalyze O_2 to generate $O_2^{\bullet-}$. TA (terephthalic acid) and WST-1 (2-(4-iodophenyl)-3-(4 -nitrophenyl)-5-(2,4-disulfophenyl)-2H -tetrazolium, monosodium salt) were used as the indicators for ·OH and $O_2^{\bullet-}$, respectively. As shown in Figure S9, the Mg20-CDs could scavenge ·OH and $O_2^{\bullet-}$effectively. The specific antioxidant activity of Mg-CDs was further investigated by EPR. As shown in Figure 3E−G, the signals of DMPO/$^{\bullet}OH$, DMPO/$O_2^{\bullet-}$, and TEMP/$^1O_2$ decreased significantly in the presence of Mg20-CDs, indicating that Mg20-CDs exhibit great scavenging capability for ·OH, $O_2^{\bullet-}$and $^1O_2$.

The possible catalytic mechanism of photoswitchable antioxidant and prooxidant activities of Mg-CDs are shown in Figure 3H. The photoinduced OXD-like activity could be attributed to the catalytic reaction of Mg-CDs in the excited state.[32] Under illumination, the valence electrons of Mg-CDs transition from the ground state (S_0) to the excited state (S_1). The electrons in the excited state could transfer to the O_2 to produce the $O_2^{\bullet-}$. Meanwhile, the excited-state Mg-CDs may reach the triplet excited state through intersystem crossing. The Mg-CDs in the triplet excited state have a relatively long lifetime and are able to undergo energy transfer with the triplet oxygen molecules in the ground state, generating singlet oxygen.[21,32,39] In contrast, the SOD-like activity of Mg-CDs could be attributed to electron transfer in the ground state.

https://doi.org/10.1021/acsami.5c05025
ACS Appl. Mater. Interfaces 2025, 17, 26467−26479

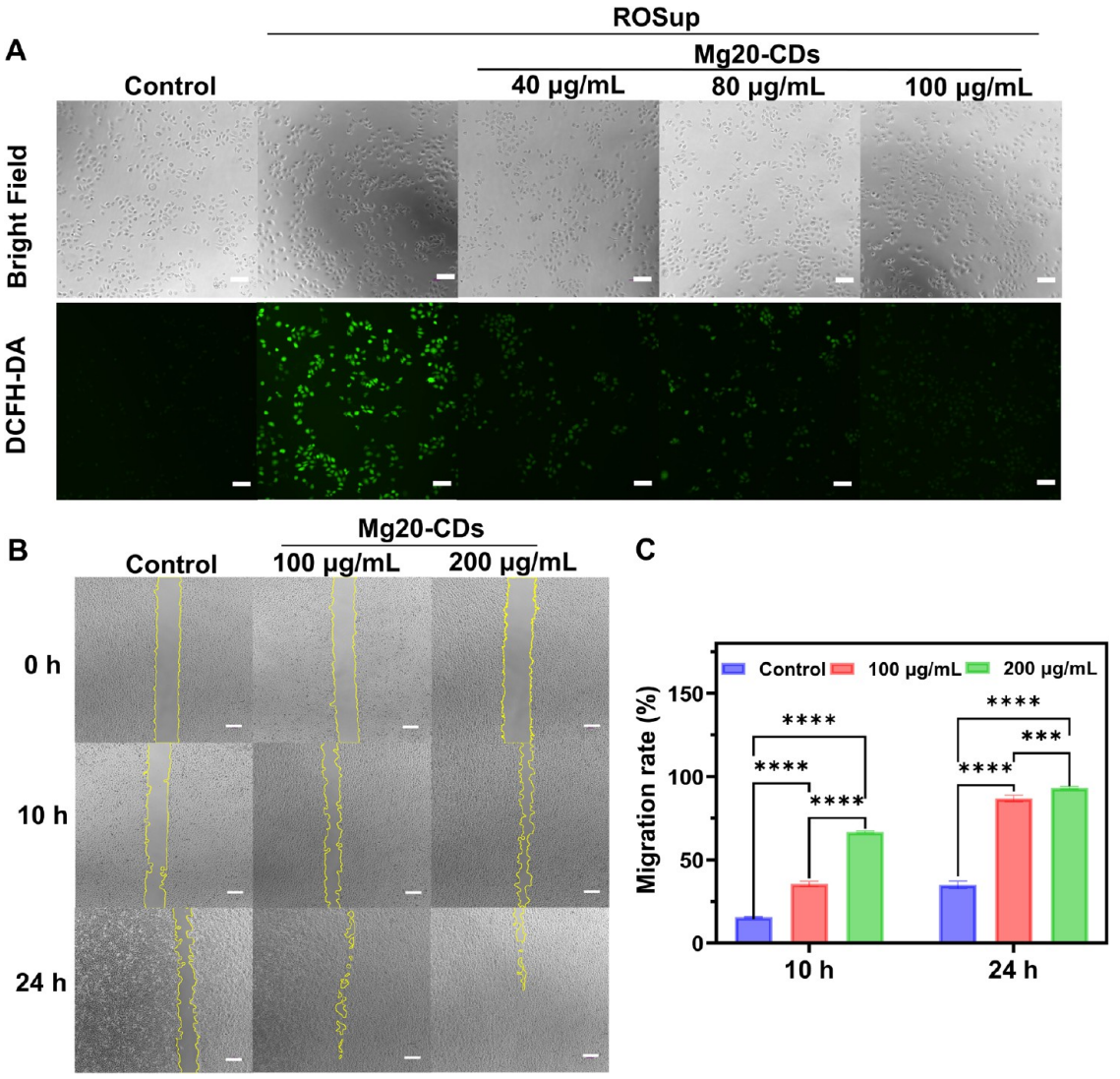

Figure 5. (A) ROS staining using DCFH-DA in HaCaT cells under different treatments as indicated (scale bar: 50 μm), (B) representative photographs of the wound gap over time in HaCaT cells treated with and without Mg20-CDs, and (C) corresponding migration rates. In panel C, data are presented as means ± SD from three independent experiments. Statistical comparisons were analyzed by Two-way ANOVA Tukey's multiple comparison test. *p < 0.05, **p < 0.01, ***p < 0.001, ****p < 0.0001, and n. s., not significant.

Without illumination, the LUMO of Mg-CDs could accept electrons from $O_2^{\bullet-}$, and the electron at HOMO could transfer to $O_2^{\bullet-}$. This electron transfer process accelerates the disproportion of $O_2^{\bullet-}$.[40,41]

The excellent photoinduced OXD-like activity of Mg20-CDs inspired us to investigate their antibacterial capability.[42] The antibacterial performance of Mg20-CDs was evaluated by using the plate counting method. *E. coli* and *S. aureus* were selected as the representative Gram-negative and Gram-positive bacteria, respectively. As shown in Figure 4A, there was no significant difference in the number of colonies between the plates with and without Mg20-CDs at a low concentration of 12.5 μg/mL in the absence of illumination. The antibacterial rate of Mg20-CDs was no more than 40% even in a high concentration of 125 μg/mL without illumination. The number of colonies of the control group showed no obvious change with illumination, which indicates that light alone does not cause damage to the bacteria. In contrast, the number of colonies on the plates with Mg20-CDs under illumination was significantly decreased with an increase in the concentration of Mg20-CDs. Colonies of various groups were quantitatively counted to assess the antibacterial activities (eq 1). The antibacterial rates of Mg20-CDs against *E. coli* and *S. aureus* were both over 99% when their concentration was 125 μg/mL, demonstrating the excellent broad-spectrum antibacterial activity of Mg20-CDs.

SEM was used to characterize the morphologies of the bacteria. As shown in Figure 4B, the typical *E. coli* and *S. aureus* exhibit complete rod shapes[43] and spherical shapes,[44] respectively, with smooth surfaces. The morphologies of both bacteria remained unchanged under only illumination, indicating that light had no effect on the morphologies of bacteria. When Mg20-CDs were added but without illumination, the morphologies remained intact. However, in the presence of Mg20-CDs and illumination, the morphology of bacteria changed significantly with surface pits, collapses, and even fragmentation. This suggests that the ROS generated by Mg20-CDs under illumination caused damage to the structures of the bacteria.

https://doi.org/10.1021/acsami.5c05025
ACS Appl. Mater. Interfaces 2025, 17, 26467−26479

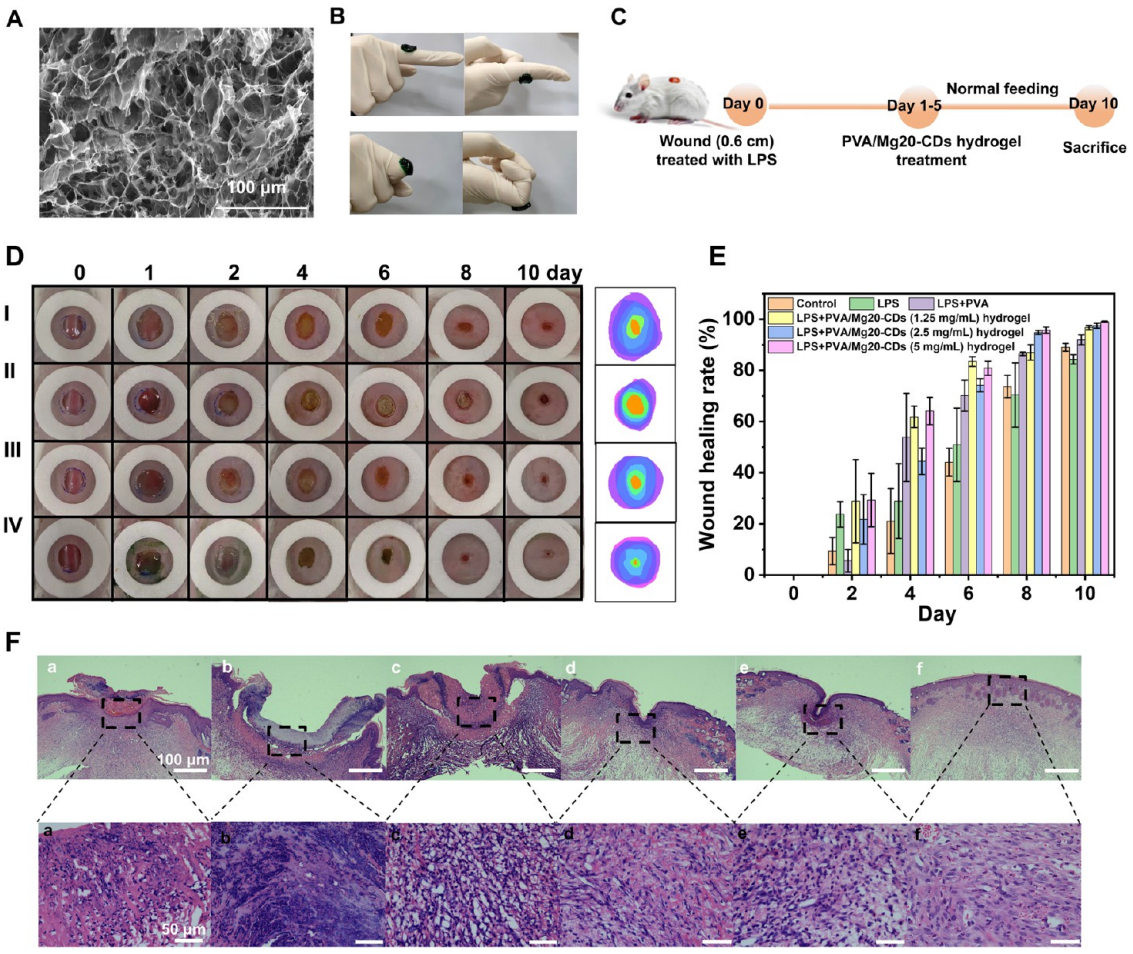

Figure 6. Capability of PVA/Mg20-CDs hydrogel to facilitate wound healing *in vivo*. (A) SEM image of PVA/Mg20-CDs hydrogel, (B) adhesion property of PVA/Mg20-CDs hydrogel, (C) diagram of PVA/Mg20-CDs hydrogel in the treatment of mice, (D) representative photographs of wounds in different treatment groups (I: control, II: LPS, III: LPS + PVA hydrogel, IV: LPS+PVA/Mg20-CDs (5 mg/mL) hydrogel), (E) wound recovery rates of various groups, and (F) hematoxylin and eosin (H&E) staining of wound tissues after treatment (a: control, b: LPS, c: LPS + PVA hydrogel, d: LPS+ PVA/Mg20-CDs (1.25 mg/mL) hydrogel, e: LPS+ PVA/Mg20-CDs (2.5 mg/mL) hydrogel, f: LPS+ PVA/Mg20-CDs (5 mg/mL)). For (D), (E), and (F), control: wound group.

Bacterial biofilms are multicellular complexes formed by the aggregation of bacteria and their secreted extracellular polymeric substances. They have a complex structure that protects bacteria from external damage. Disrupting bacteria within the biofilm is critically important to wound healing.[45] The excellent antibacterial capability of Mg20-CDs inspired us to further investigate their application in biofilm elimination. Crystal violet (CV) is a basic dye that can stain bacterial biofilm to appear blue, allowing direct observation of the presence and distribution of the biofilm. So, the inhibition efficacy of Mg20-CDs against biofilms was investigated using the CV staining method.[46] The color changed significantly from blue to pale blue with the increase of the concentration of Mg20-CDs, which indicates the remarkable biofilm elimination of Mg20-CDs (Figure S10). The biofilm inhibition efficiencies for *E. coli* and *S. aureus* were calculated to be c.a. 90%%, respectively.

Based on the antioxidant activity of Mg20-CDs, we further investigated their ROS-scavenging capacity *in vitro*. First, the biocompatibility of Mg20-CDs *in vitro* was evaluated by using the cell counting kit-8 (CCK-8) and hemolysis tests. As shown in Figure S11A, even at a high concentration of 200 μg/mL, the viability of HaCaT cells was over 90%. Furthermore, the results of the hemolysis test indicated that a hemolysis rate of <3% was observed even at a high concentration of Mg20-CDs (125 μg/mL) (Figure S11B). The results demonstrated that Mg20-CDs exhibited good biocompatibility. We also investigated the stability of the Mg20-CDs under physiological conditions. As shown in Figure S12, the UV−vis adsorption and the fluorescence spectra of Mg-CDs at different pH values show no obvious difference, indicating the good stability of Mg-CDs under the physiological pH range. The ROS-specific green emission fluorescent probe (DCFH-DA), which can be oxidized into fluorescent DCF in the presence of ROS, was used to evaluate the ROS-scavenging capacity of the Mg20-CDs. ROSup induced the increase of the ROS level within HaCaT cells. As shown in Figure 5A, the cells treated with ROSup alone showed much brighter green fluorescence compared with the control group, indicating that the ROS level in the living cells was increased successfully. Whereas the cells pretreated with Mg20-CDs showed weak green fluorescence, indicating that Mg20-CDs scavenged the ROS induced by ROSup.

Cells remodel the tissue microenvironment by migrating to the site of injury and then proliferating.[47] The regeneration of damaged tissue is largely dependent on cell migration. Hence,

https://doi.org/10.1021/acsami.5c05025
ACS Appl. Mater. Interfaces 2025, 17, 26467−26479

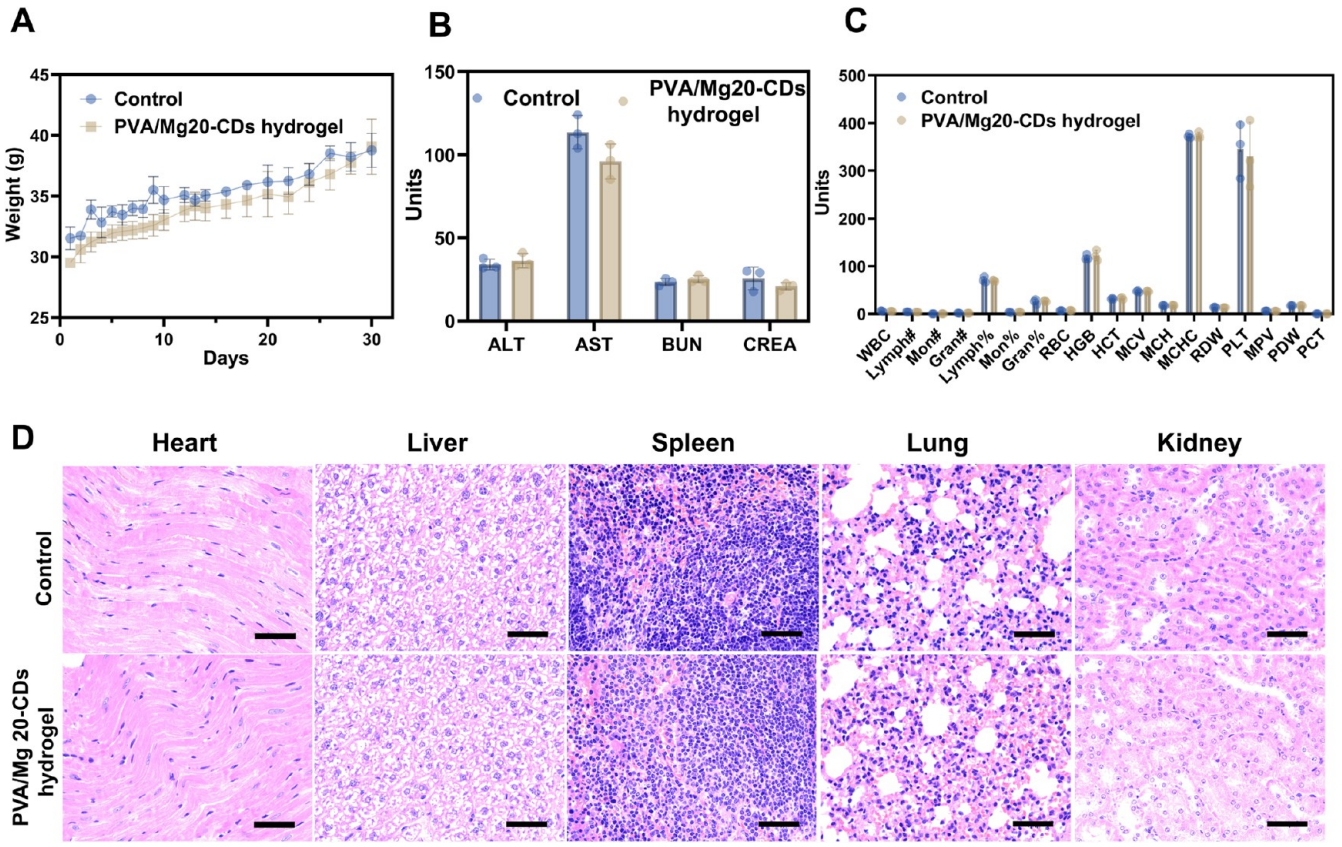

Figure 7. *In vivo* biosafety evaluation of PVA/Mg20-CDs hydrogels. (A) Body weight change, (B) blood biochemical analysis, (C) blood routine, and (D) H&E staining images of the heart, liver, spleen, lung, and kidney of mice treated with and without PVA/Mg20-CDs hydrogels. In panels (A−C), data are presented as means ± SD from three independent experiments. The scale bar in panel (D) is 50 μm.

HaCaT cells were mechanically scratched to simulate a wound and then incubated with Mg20-CDs for 24 h to evaluate their wound healing ability *in vitro* (the cell migration rates were calculated according to eq 2). As shown in Figure 5B,C, Mg20-CDs significantly promoted cell migration with a rate of over 80%. This indicated that Mg20-CDs, which facilitated the migration of HaCaT cells, showed great potential in accelerating wound healing.

Based on the excellent SOD-like activity *in vitro* and remarkable biocompatibility of Mg20-CDs, we tried to use Mg20-CDs for the treatment of acute inflammation wounds. All animal experiments were approved by the Animal Protection and Utilization Committee of Chongqing University (Approval Number: CQU-IACUC-RE-202502-002). Hydrogel is an ideal wound dressing due to its nontoxicity, good biocompatibility, and appropriate mechanical properties. Poly(vinyl alcohol) (PVA) is a synthetic polymer with hydrophilic groups that has attracted considerable attention due to its excellent biocompatibility. Physical cross-linking is one of the mechanisms for gelation in PVA hydrogels, involving the formation of strong hydrogen bonds between polymer chains to create microcrystals.[48] This can be achieved through repeated freeze−thaw cycles, resulting in hydrogels with nontoxic residues. The hydrogels prepared by this method exhibit good biodegradability, tissue-like viscoelasticity, and excellent stability at room temperature. Therefore, we combined PVA and Mg20-CDs to prepare a hydrogel to facilitate healing of the wound.

Figure 6A demonstrates that the PVA/Mg20-CDs hydrogel possesses a porous and interconnected network. The porous structure allows them to act as a flexible backbone, while the interconnected network enhances hydrogen bonding interaction, thereby improving the mechanical properties of the hydrogel.[49] Additionally, hydrogels used for wound dressing should adhere tightly to the skin during the treatment process and not easily fall off, providing a stable environment for the wound.[50] Therefore, we evaluated the adhesion of the PVA/Mg20-CDs hydrogel by bending and straightening the finger joints, as shown in Figure 6B. The hydrogels adhered well to the finger joints regardless of their position or movement state, demonstrating their excellent adhesion properties.

As shown in Figure 6C, an acute inflammation wound mouse model was established by creating a circular wound of 0.6 cm × 0.6 cm on the back of each mouse and then treating the wound with LPS. The mice were then treated with PVA/Mg20-CDs hydrogels for five consecutive days. Photos of the mice's backs were collected daily to record the wound sizes. Figures 6D and S13 show that the wounds induced by LPS exhibited significant redness and edema compared to control wounds. The wounds treated with PVA/Mg20-CDs hydrogels showed markedly less redness and edema compared with other groups, and the healing rate was fastest (Figure 6E). After 10 days, the mice were sacrificed, and the skin on the mice's back was collected for H&E staining. The results of H&E staining (Figure 6F) showed that the healing rate of inflammation wound induced by LPS was the slowest, and the number of inflammatory cells, such as lymphocytes with large and deeply stained nuclei, was the highest. Nevertheless, the healing rate of the group treated with PVA/Mg20-CDs hydrogels was the fastest, and the number of inflammatory cells was significantly

https://doi.org/10.1021/acsami.5c05025
ACS Appl. Mater. Interfaces 2025, 17, 26467−26479

reduced. These results indicated that the PVA/Mg20-CDs hydrogels exhibited an anti-inflammatory capacity and facilitated wound healing.

We also investigated the distribution of Mg20-CDs released from PVA/Mg20-CDs hydrogels on the wounds in mice (Figure S14). The results indicated that after 2 h, the maximum fluorescence of Mg20-CDs was detected in the whole body of the mice. Moreover, the major organs, including heart, liver, spleen, lung, and kidney, were collected at 2 h. As shown in Figure S14B, negligible fluorescence from these organs was observed, indicating that Mg20-CDs did not accumulate in these organs of the mice. After 12 h, no significant fluorescence was detected, suggesting that Mg20-CDs had almost been almost metabolized.

The biosafety of PVA/Mg20-CDs hydrogels *in vivo* was assessed. As shown in Figure 7A, the weight trends of mice treated with PVA/Mg20-CDs hydrogels were consistent with those of healthy mice over the 30-day period. Figure 7B shows that there were no significant differences in the levels of alanine aminotransferase (ALT), aspartate aminotransferase (AST), blood urea nitrogen (BUN), and creatinine (CREA) between mice treated with PVA/Mg20-CDs hydrogels and healthy mice, indicating that PVA/Mg20-CDs hydrogels had no obvious toxicity to the liver and kidney. Moreover, the results of the blood routine showed that there was no significant difference between the group treated with PVA/Mg20-CDs hydrogels and the healthy group (Figure 7C). Additionally, the main organs (heart, liver, spleen, lung, and kidney) were collected for H&E staining to further evaluate the safety of PVA/Mg20-CDs hydrogels. As shown in Figure 7D, no obvious organ damage was observed in the mice treated with the PVA/Mg20-CDs hydrogels. These results demonstrated that PVA/Mg20-CDs hydrogels possessed good biocompatibility.

3. CONCLUSIONS

In this work, Mg-doped CDs with photoswitchable antioxidatant and prooxidant activities were designed as antibacterial and anti-inflammation agents. Under illumination, the Mg-CD nanozymes exhibiting photoinduced OXD-like activity could catalyze the production of ROS, *e.g.*, $O_2^{\bullet-}$ and , through electron and energy transfer in the excited state. The photoinduced OXD-like activity of Mg-CDs can be used for antibacterial and antibiofilm. Without illumination, the Mg-CDs exhibited high SOD-like activity and robust scavenging capacities for $^1O_2$ and $^\bullet$OH. The Mg-CDs could scavenge ROS *in vitro* and *in vivo*, remodel tissue microenvironment by facilitating the migration of HaCaT cells, and finally boost the healing of inflammation wounds caused by LPS. Furthermore, the Mg-CDs exhibited excellent biocompatibility. These findings enable switching the antioxidant and prooxidant activities of CD nanozymes by illumination under physiological conditions, expanding the biomedical application of nanozymes.

4. EXPERIMENTAL SECTION

4.1. Synthesis of Mg-CDs. Based on our previous work, a one-step solvothermal method was used to synthesize a series of Mg-CDs. After uniformly mixing $MgCl_2{\cdot}6H_2O$ (0, 2.5, 5, 10, 20, 40, 80 mg), glutathione (reduced) (0.7 g), and formamide (70 mL), the mixture was added into a reactor. Then, the mixture was heated at 160 °C for 8 h. The obtained solution was dialyzed for 7 days using a 3500-Da dialysis bag. After the dialysis and purification, most of the solvent was removed by rotary evaporation. Then, the concentrated solution was centrifuged (10000 rpm, 10 min) to remove precipitates. The freeze−thaw and centrifugation steps were repeated. After that, the solution was filtered through a 0.22 μm filter membrane. Finally, vacuum freeze-drying was performed for approximately 72 h to obtain a dry green powder, which is the purified Mg-CDs.

4.2. Measurement of Photoinduced OXD-like Activity. A 13-W LED lamp or a 300 W Xe lamp was used to test the photoinduced OXD-like activity of CDs and Mg-CDs, and the control group was placed in the chemistry laboratory in an ordinary lighting environment. The light intensities relevant to this work are shown in Table S6. The maximum initial velocity (V_{max}) and Michaelis−Menten constant (K_m) were used to analyze the kinetic parameters of Mg20-CDs. These kinetic results were obtained at varied concentrations of TMB. Briefly, 500 μL of TMB with different concentrations was mixed with 500 μL of Mg20-CDs (5 μg/mL), and the mixture was illuminated under a 300 W Xe lamp every 2 s for a total of 30 s.

4.3. Measurement of SOD-like Activity. The total superoxide dismutase assay kit (S311, Dojindo Molecular Technologies, Inc.) was used to evaluate the SOD-like activity of Mg-CDs. In this assay, WST-1 (2-(4-iodophenyl)-3-(4-nitrophenyl)-5-(2,4-disulfo-phenyl)-2H-tetrazolium, monosodium salt) was utilized. WST-1 reacts with the superoxide anion, resulting in the generation of formazan dye that has an absorbance peak at 450 nm. The SOD or its mimetics inhibits this reaction. The inhibition rate of SOD (%) was calculated according to the equation

$$\text{the inhibition rate of SOD (\%)} = \frac{(A_{\text{Control 1}} - A_{\text{Control 3}}) - (A_{\text{Sample}} - A_{\text{Control 2}})}{(A_{\text{Control 1}} - A_{\text{Control 3}})} \times 100$$

Control 1: coloring without inhibitor, Control 2: sample blank, and Control 3: reagent blank.

Serial dilutions of the sample were carried out to establish an inhibition curve, and the concentration associated with 50% inhibition (IC_{50}) was ascertained. A unit (1 U) of SOD-like activity is defined as the quantity of enzyme within 20 μL of the sample that inhibits the reduction reaction of WST-1 with a superoxide anion by 50%. Then, the SOD activity (U/mg) of the sample could be calculated according to the concentration at IC_{50}.

4.4. Electron Paramagnetic Resonance (EPR). EPR measurement for $^1O_2$ and $O_2^{\bullet-}$ production was carried out as follows: 100 μL of TEMP or DMPO (100 mM) was mixed with 100 μL of Mg20-CDs (1 mg/mL), respectively. The mixtures were treated in the dark or under illumination for 10 min for EPR measurement.

EPR measurement was conducted for the ROS-scavenging capability of Mg20-CDs. The hydroxyl radical was produced by reacting 100 μL of $FeSO_4$ (5 mg/mL) and 10 μL of 30% H_2O_2 in water for 5 min. The singlet oxygen was produced by mixing 100 μL of 6% NaClO with 100 μL of 50 mM H_2O_2. The superoxide anion was produced by mixing 20 μL of 10 mM xanthine solution with 20 μL of 1 U/mL xanthine oxidase in PBS buffer. DMPO was used to trap $^\bullet$OH and $O_2^{\bullet-}$ to generate the spin adducts (DMPO/$^\bullet$OH) and (DMPO/$O_2^{\bullet-}$), respectively. TEMP was used to trap singlet oxygen. EPR spectra were recorded in the absence and presence of Mg20-CDs.

4.5. Antibacterial Activity Of Mg20-CDs *In Vitro*. Bacteria culture: A single colony of *E. coli* (ATCC 25922) was inoculated into 100 mL of LB medium and cultivated overnight at 37 °C with shaking at 150 rpm. The bacterial concentration was estimated by measuring the optical density (OD) of the bacterial suspension at 600 nm. The same method was used to culture *S. aureus* (ATCC 25923).

Antibacterial assay on plates: 1 mL of bacteria suspension (~1 × 10^7 CFU/mL) was mixed with 0.9% NaCl solution and Mg20-CDs (final concentration of 12.5, 25, 50, 100, 125 μg/mL, in 0.9% NaCl solution), respectively, and illuminated under Xe lamp for 5 min. The solutions were then diluted 10^3 times, and 20 μL of the diluted bacterial solution was spread on the LB agar plate and incubated overnight at 37 °C. The antibacterial rate was calculated by counting

https://doi.org/10.1021/acsami.5c05025
ACS Appl. Mater. Interfaces 2025, 17, 26467−26479

the number of colonies on the plate. The formula for calculating the antibacterial rate is as follows:

$$\text{antibacterial rate (\%)} = (\text{CFU control} - \text{CFU test})/\text{CFU control} \times 100\% \quad (1)$$

SEM characterization of bacterial morphologies: SEM was used to characterize the morphologies of bacteria. After treatment with Mg20-CDs (125 μg/mL) under light illumination, *E. coli* (ATCC 25922) and *S. aureus* (ATCC 25923) were collected by centrifugation at 3000 rpm for 10 min at 4 °C. The bacterial pellets were washed three times with PBS. Following the fixation of glutaraldehyde, gradient dehydration was performed using ethanol solution (30, 50, 70, 90, and 100%). Finally, the samples were dripped onto silicon wafers, vacuum-dried, and imaged using a SEM.

Biofilm elimination *in vitro*: Single colonies of *E. coli* (ATCC 25922) and *S. aureus* (ATCC 25923) were inoculated into LB liquid medium and cultivated with shaking at 150 rpm at 37 °C overnight. 1 mL of bacterial suspension (~1×10^7 CFU/mL) was added to each well of a 12-well plate and incubated statically at 37 °C for 48 h, with fresh LB liquid medium replaced every 24 h. After the biofilm formation, 1 mL of Mg20-CDs diluted in LB medium (at concentrations of 12.5, 25, 50, 100, and 125 μg/mL) was added to each well, and the plates were illuminated under a Xe lamp for 5 min, followed by continued incubation for 24 h. After 24 h, the medium and planktonic bacteria were discarded, and the wells were washed three times with 0.9% NaCl. The biofilms were then fixed with 95% ethanol for 15 min. Subsequently, 1 mL of crystal violet was added to stain the biofilm for 5 min. Excess crystal violet was washed away with 0.9% NaCl, and crystal violet bound to the biofilm was dissolved in 10% acetic acid. The absorbance of crystal violet at 590 nm was measured to assess the biofilm elimination ability of Mg20-CDs.

All antibacterial experiments in this work were performed by using a 300 W Xe lamp with an illumination time of 5 min. The control groups were placed in an ordinary lighting environment.

4.6. *In Vitro* Biosafety Evaluation of Mg20-CDs. Cellular toxicity evaluation: The Cell Counting Kit-8 (CCK-8) was used to assess the cellular toxicity of Mg-CDs. HaCaT (human immortalized keratinocytes) cells were seeded into a 96-well plate at a density of 1×10^4 cells per well and incubated with Mg20-CDs at various concentrations (0, 20, 40, 60, 80, 100, 150, and 200 μg/mL) at 37 °C for 24 h. After incubation, the cells were washed three times with PBS, and 10 μL of a CCK-8 solution was added to each well. The cells were then incubated in the dark for an additional 1 h. The cell viability was evaluated by measuring the absorbance at 450 nm.

Hemolysis test: Whole blood was collected from mice and centrifuged at 5000 rpm for 5 min at 4 °C. The erythrocytes were then washed three times with PBS until the supernatant was colorless. Next, 30 μL of Mg20-CDs at different concentrations (12.5, 25, 50, 100, and 125 μg/mL) was added to a 2% erythrocyte suspension in PBS and incubated for 4 h at 37 °C. The resultant solutions were centrifuged to collect supernatant, and the absorbance at 570 nm was measured.

4.7. Intercellular ROS Scavenging in HaCaT Cells. The scavenging capability of the ROS scavenger in cells was measured by using the fluorescent probe 2′,7′-dichlorfluorescein diacetates (DCFH-DA). Briefly, HaCaT cells in the logarithmic growth phase were seeded into a 96-well plate at a density of 5×10^3 cells per well and allowed to adhere overnight. Different concentrations of Mg20-CDs (20, 40, 80, 100 μg/mL) diluted in RPMI 1640 were added to the cells for continued culture for 7 h. The medium was discarded, and the cells were incubated with ROSup (50 μg/mL) for 30 min. After discarding the ROSup-containing medium, DCFH-DA (at a dilution ratio of 1:1000) was added and incubated for another 30 min. Following the incubation, excess DCFH-DA was washed away with PBS, and cell images were observed under a fluorescence microscope.

4.8. Cell Wound Healing Assay. HaCaT cells in the logarithmic growth phase were seeded into a 6-well plate with a density of 5×10^5 cells per well and allowed to adhere overnight. A straight scratch was made in the cell monolayer using a 200 μL pipette tip. The cell debris was washed away with PBS after scratching. The control group was supplemented with serum-free medium, and the test group was added with Mg20-CDs solutions diluted in serum-free medium. This was marked as 0 h. The width of the scratch was observed and imaged by a microscope at the 10th and 24th hour. The cell migration rate was calculated using the following formula:

$$\text{cell migration rate} = \frac{L_t - L_0}{L_0} \times 100\% \quad (2)$$

where L_0 and L_t mean the width of the scratch at time points of 0 and t, respectively.

4.9. SEM of PVA/Mg20-CDs Hydrogel. The freeze-dried PVA/Mg20-CDs hydrogel was put into liquid nitrogen to make it break rapidly, and PVA/Mg20-CDs hydrogel fragments with cross sections were obtained. The fragments were fixed and coated with Au, and then the SEM images of PVA/Mg20-CDs hydrogel were captured.

4.10. PVA/Mg20-CDs Facilitates LPS-Induced Acute Inflammatory Wound Healing. All animal experiments were approved by the Animal Protection and Utilization Committee of Chongqing University (Approval Number: CQU-IACUC-RE-202502-002). Mice were purchased from Hunan Slike Jingda Experimental Animal Co., Ltd. Female Kunming mice (6−8 weeks old, 30 g) with shaved backs were subjected to full-thickness circular wounds (0.6 cm in diameter) on their backs. Subsequently, 50 μL of a 5 mg/mL LPS solution was applied dropwise to the wound tissue, followed by the application of PVA/Mg-CDs hydrogel on the wound site using a dressing. The mice were divided into six groups: wound group, wound + LPS, wound + LPS + PVA hydrogel, wound + LPS + PVA/Mg20-CDs (1.25 mg/mL) hydrogel, wound + LPS + PVA/Mg20-CDs (2.5 mg/mL) hydrogel, and wound + LPS + PVA/Mg20-CDs (5 mg/mL) hydrogel. The healing of the skin wounds was observed and photographed daily, with dressings changed daily for five consecutive days. Ten days later, the mice were sacrificed, and their dorsal skin tissues were collected. After fixation in paraformaldehyde for 24 h, the skin tissues were stained with hematoxylin and eosin (H&E) staining to assess the pathological conditions of each group.

4.11. Investigation of Mg20-CDs Circulation *In Vivo*. Female Kunming mice (6−8 weeks old, 30 g) with shaved backs were subjected to full-thickness circular wounds (0.6 cm in diameter) on their backs. Subsequently, live imaging of the mice was performed at 1, 2, 4, 6, and 12 h after the application of PVA/Mg20-CDs hydrogel on their wounds.

4.12. Biocompatibility of PVA/Mg20-CDs Hydrogel *In Vivo*. Healthy female Kunming mice with full-thickness circular wounds (0.6 cm in diameter) on their backs were divided into a control group and a PVA/Mg20-CDs (5 mg/mL) hydrogel group. The PVA/Mg20-CDs hydrogel group received continuous treatments for 5 days. The body weight of the mice was monitored daily. After 30 days of normal feeding, the mice were euthanized. Blood samples were collected for blood routine examination and blood biochemistry analysis. Additionally, major organs (heart, liver, spleen, lungs, and kidneys) were collected and sectioned for H&E staining.

4.13. Statistical Analysis. One-way analysis of variance (ANOVA) and Two-way ANOVA Tukey's multiple comparison tests were used to determine the statistical significance ($^*p < 0.05$, $^{**}p < 0.01$, $^{***}p < 0.001$, and $^{****}p < 0.0001$, and n. s., not significant), and a p-value of less than 0.05 was considered statistically significant.

■ ASSOCIATED CONTENT

Supporting Information

The Supporting Information is available free of charge at https://pubs.acs.org/doi/10.1021/acsami.5c05025.

Regents, instruments, the XPS survey, the TEM image of CDs, the UV−vis spectra, the QYs, and fluorescence lifetime of CDs and Mg-CDs (PDF)

https://doi.org/10.1021/acsami.5c05025
ACS Appl. Mater. Interfaces 2025, 17, 26467−26479

AUTHOR INFORMATION

Corresponding Authors

Chuan-Hua Zhou − *National Demonstration Center for Experimental Chemistry and Chemical Engineering Education (Yunnan University), School of Chemical Science and Technology, Yunnan University, Kunming 650091, P. R. China*; Email: chzhou@ynu.edu.cn

Zhining Xia − *Chongqing Key Laboratory of Natural Product Synthesis and Drug Research, Innovative Drug Research Center, School of Pharmaceutical Sciences, Chongqing University, Chongqing 400044, P. R. China*; Email: znxia@cqu.edu.cn

Dai-Wen Pang − *State Key Laboratory of Medicinal Chemical Biology, Frontiers Science Centre for New Organic Matter, Tianjin Key Laboratory of Biosensing and Molecular Recognition, Research Centre for Analytical Sciences, College of Chemistry, Frontiers Science Center for Cell Responses, Nankai University, Tianjin 300071, P. R. China*; orcid.org/0000-0002-7017-5725; Email: dwpang@whu.edu.cn

Cui Liu − *Chongqing Key Laboratory of Natural Product Synthesis and Drug Research, Innovative Drug Research Center, School of Pharmaceutical Sciences, Chongqing University, Chongqing 400044, P. R. China*; orcid.org/0000-0002-8399-5765; Email: liucui@cqu.edu.cn

Authors

Jinyu Shi − *Chongqing Key Laboratory of Natural Product Synthesis and Drug Research, Innovative Drug Research Center, School of Pharmaceutical Sciences, Chongqing University, Chongqing 400044, P. R. China; National Demonstration Center for Experimental Chemistry and Chemical Engineering Education (Yunnan University), School of Chemical Science and Technology, Yunnan University, Kunming 650091, P. R. China*

Yu Zhang − *Chongqing Key Laboratory of Natural Product Synthesis and Drug Research, Innovative Drug Research Center, School of Pharmaceutical Sciences, Chongqing University, Chongqing 400044, P. R. China; College of Life Sciences and Health, Wuhan University of Science and Technology, Wuhan 430065, P. R. China*

Xiangyang Fang − *Chongqing Key Laboratory of Natural Product Synthesis and Drug Research, Innovative Drug Research Center, School of Pharmaceutical Sciences, Chongqing University, Chongqing 400044, P. R. China; National Demonstration Center for Experimental Chemistry and Chemical Engineering Education (Yunnan University), School of Chemical Science and Technology, Yunnan University, Kunming 650091, P. R. China*

Xing Fan − *Department of Pathology, the First Affiliated Hospital of Xi'an Jiaotong University, Xi'an, Shaanxi 710061, P. R. China*

Jing Li − *Chongqing Key Laboratory of Natural Product Synthesis and Drug Research, Innovative Drug Research Center, School of Pharmaceutical Sciences, Chongqing University, Chongqing 400044, P. R. China; National Demonstration Center for Experimental Chemistry and Chemical Engineering Education (Yunnan University), School of Chemical Science and Technology, Yunnan University, Kunming 650091, P. R. China*

Complete contact information is available at: https://pubs.acs.org/10.1021/acsami.5c05025

Author Contributions

#J.S. and Y.Z. contributed equally to this work.

Notes

The authors declare no competing financial interest.

ACKNOWLEDGMENTS

This work was supported by the National Natural Science Foundation of China (32171392), the Fundamental Research Funds for the Central Universities (2024CDJXY002 and 2024CDIQYJCY1-001), and the Natural Science Foundation of Chongqing (CSTB2024NSCQ-MSX0390). The authors also thank Dr. Kai Zhou at the Analytical and Testing Center of Chongqing University for assisting with XPS measurement.

REFERENCES

(1) Singh, N.; Sherin, G. R.; Mugesh, G. Antioxidant and Prooxidant Nanozymes: From Cellular Redox Regulation to Next-Generation Therapeutics. *Angew. Chem., Int. Ed.* **2023**, *62* (33), No. e202301232.

(2) Shahraki, S.; Vaziri, E.; Saboury, A. A.; Fan, K. Biomedical potential of nanozymes: Harnessing redox enzyme mimicry for theranostic applications. *Coord. Chem. Rev.* **2024**, *517*, No. 215937.

(3) Huang, Y.; Ren, J.; Qu, X. Nanozymes: Classification, Catalytic Mechanisms, Activity Regulation, and Applications. *Chem. Rev.* **2019**, *119* (6), 4357−4412.

(4) Zhao, H.; Zhang, R.; Yan, X.; Fan, K. Superoxide dismutase nanozymes: an emerging star for anti-oxidation. *J. Mater. Chem.B* **2021**, *9* (35), 6939−6957.

(5) Shah, J.; Pandya, A.; Goyal, P.; Misra, S. K.; Singh, S. BSA-Decorated Magnesium Nanoparticles for Scavenging Hydrogen Peroxide from Human Hepatic Cells. *ACS Appl. Nano Mater.* **2020**, *3* (4), 3355−3370.

(6) Xiao, Y.; Zhang, M.; Lu, N. Fluorescent Fingerprint Identification of Protein Structural Changes and Disease-Specific Amyloid Beta Aggregates Based on a Single-Nanozyme Sensor Array. *Anal. Chem.* **2025**, *97* (9), 4978−4986.

(7) Gao, L.; Zhuang, J.; Nie, L.; Zhang, J.; Zhang, Y.; Gu, N.; Wang, T.; Feng, J.; Yang, D.; Perrett, S.; Yan, X. Intrinsic peroxidase-like activity of ferromagnetic nanoparticles. *Nat. Nanotechnol.* **2007**, *2* (9), 577−583.

(8) Chen, J.; Ma, Q.; Li, M.; Chao, D.; Huang, L.; Wu, W.; Fang, Y.; Dong, S. Glucose-oxidase like catalytic mechanism of noble metal nanozymes. *Nat. Commun.* **2021**, *12*, No. 3375.

(9) Liu, Q.; Zhang, A.; Wang, R.; Zhang, Q.; Cui, D. A Review on Metal- and Metal Oxide-Based Nanozymes: Properties, Mechanisms, and Applications. *Nano-Micro Lett.* **2021**, *13*, No. 154.

(10) Sun, H.; Zhou, Y.; Ren, J.; Qu, X. Carbon Nanozymes: Enzymatic Properties, Catalytic Mechanism, and Applications. *Angew. Chem., Int. Ed.* **2018**, *57*, 9224−9237.

(11) Sun, Y.; Xu, B.; Pan, X.; Wang, H.; Wu, Q.; Li, S.; Jiang, B.; Liu, H. Carbon-based nanozymes: Design, catalytic mechanism, and bioapplication. *Coord. Chem. Rev.* **2023**, *475*, No. 214896.

(12) Sheng, J.; Wu, Y.; Ding, H.; Feng, K.; Shen, Y.; Zhang, Y.; Gu, N. Multienzyme-Like Nanozymes: Regulation, Rational Design, and Application. *Adv. Mater.* **2023**, *36* (10), No. 2211210.

(13) Biswas, S.; Tripathi, P.; Kumar, N.; Nara, S. Gold nanorods as peroxidase mimetics and its application for colorimetric biosensing of malathion. *Sens. Actuators, B* **2016**, *231*, 584−592.

(14) Estelrich, J.; Busquets, M. A. Prussian Blue: A Nanozyme with Versatile Catalytic Properties. *Int. J. Mol. Sci.* **2021**, *22* (11), 5993.

(15) Qin, Z. G.; Chen, B.; Mao, Y.; Shi, C.; Li, Y.; Huang, X.; Yang, F.; Gu, N. Achieving Ultrasmall Prussian Blue Nanoparticles as High-Performance Biomedical Agents with Multifunctions. *ACS Appl. Mater. Interfaces* **2020**, *12* (51), 57382−57390.

(16) Sun, X.; Luo, S.; Zhang, L.; Miao, Y.; Yan, G. Photodynamic antibacterial activity of oxidase-like nanozyme based on long-lived room-temperature phosphorescent carbon dots. *Food Chem.* **2024**, *434*, No. 137541.

(17) Tang, G.; He, J.; Liu, J.; Yan, X.; Fan, K. Nanozyme for tumor therapy: Surface modification matters. *Exploration* **2021**, *1* (1), 75−89.
(18) Zhang, R.; Chen, L.; Liang, Q.; Xi, J.; Zhao, H.; Jin, Y.; Gao, X.; Yan, X.; Gao, L.; Fan, K. Unveiling the active sites on ferrihydrite with apparent catalase-like activity for potentiating radiotherapy. *Nano Today* **2021**, *41*, No. 101317.
(19) He, W.; Wu, J.; Liu, J.; Li, J. Single-Atom Nanozymes for Catalytic Therapy: Recent Advances and Challenges. *Adv. Funct. Mater.* **2024**, *34* (16), No. 2312116.
(20) Cheng, F.; Kotha, S.; Fu, M.; Yang, Q.; Wang, H.; He, W.; Mao, X. Nanozyme enabled protective therapy for neurological diseases. *Nano Today* **2024**, *54*, No. 102142.
(21) Zhang, J.; Liu, J. Light-activated nanozymes: catalytic mechanisms and applications. *Nanoscale* **2020**, *12* (5), 2914−2923.
(22) Liu, Y. F.; Wang, X. Y.; Wei, H. Light-responsive nanozymes for biosensing. *Analyst* **2020**, *145* (13), 4388−4397.
(23) Sancar, A. Mechanisms of DNA Repair by Photolyase and Excision Nuclease (Nobel Lecture). *Angew. Chem., Int. Ed.* **2016**, *55* (30), 8502−8527.
(24) Sorigué, D.; Légeret, B.; Cuiné, S.; Blangy, S.; Moulin, S.; Billon, E.; Richaud, P.; Brugière, S.; Couté, Y.; Nurizzo, D.; Müller, P.; Brettel, K.; Pignol, D.; Arnoux, P.; Li-Beisson, Y.; Peltier, G.; Beisson, F. An algal photoenzyme converts fatty acids to hydrocarbons. *Science* **2017**, *357* (6354), 903−907.
(25) Gabruk, M.; Mysliwa-Kurdziel, B. Light-Dependent Protochlorophyllide Oxidoreductase: Phylogeny, Regulation, and Catalytic Properties. *Biochemistry* **2015**, *54* (34), 5255−5262.
(26) Ho, M. Y.; Shen, G. Z.; Canniffe, D. P.; Zhao, C.; Bryant, D. A. Light-dependent chlorophyll f synthase is a highly divergent paralog of PsbA of photosystem II. *Science* **2016**, *353* (6302), No. aaf9178.
(27) He, L.; Li, Z.; Gu, M.; Li, Y.; Yi, C.; Jiang, M.; Yu, X.; Xu, L. Intelligent Carbon Dots with Switchable Photo-Activated Oxidase-Mimicking Activity and pH Responsive Antioxidant Activity Adaptive to the Wound Microenvironment for Selective Antibacterial Therapy. *Adv. Sci.e* **2024**, *11* (40), No. 2406681.
(28) Gallareta-Olivares, G.; Rivas-Sanchez, A.; Cruz-Cruz, A.; Hussain, S. M.; González-González, R. B.; Cárdenas-Alcaide, M. F.; Iqbal, H. M. N.; Parra-Saldívar, R. Metal-doped carbon dots as robust nanomaterials for the monitoring and degradation of water pollutants. *Chemosphere* **2023**, *312*, No. 137190.
(29) Li, X.; Fu, Y.; Zhao, S.; Xiao, J.; Lan, M.; Wang, B.; Zhang, K.; Song, X.; Zeng, L. Metal ions-doped carbon dots: Synthesis, properties, and applications. *Chem. Eng. J.* **2022**, *430*, No. 133101.
(30) Lin, L.; Luo, Y.; Tsai, P.; Wang, J.; Chen, X. Metal ions doped carbon quantum dots: Synthesis, physicochemical properties, and their applications. *TrAC Trends Anal. Chem.* **2018**, *103*, 87−101.
(31) Pandya, A.; Tripathi, A.; Purohit, R.; Singh, S.; Nandasiri, M. I.; Karakoti, A.; Singh, S. P.; Shanker, R. Fluorescent magnesium nanocomplex in a protein scaffold for cell nuclei imaging applications. *RSC Adv.* **2015**, *5* (114), 94236−94240.
(32) Shi, J.; Li, J.; Li, X.; Zhang, Y.; Hu, J.; Ning, Y.; Zhou, C.-H.; Xia, Z.; Liu, C. Coordination of Mg(II) Enhancing Photoinduced Oxidase-Like Activity of Carbon Dots for Efficient Degradation of Organic Dyes. *Chem. Mater.* **2025**, *37*, 2290−2301.
(33) Liu, C.; Fan, W.; Cheng, W.-X.; Gu, Y.; Chen, Y.; Zhou, W.; Yu, X.-F.; Chen, M.; Zhu, M.; Fan, K.; Luo, Q.-Y. Red Emissive Carbon Dot Superoxide Dismutase Nanozyme For Bioimaging And Ameliorating. *Adv. Funct. Mater.* **2023**, *33* (19), No. 2370116.
(34) Liu, C.; Bao, L.; Yang, M.; Zhang, S.; Zhou, M.; Tang, B.; Wang, B.; Liu, Y.; Zhang, Z.-L.; Zhang, B.; Pang, D.-W. Surface Sensitive Photoluminescence of Carbon Nanodots: Coupling Between the Carbonyl Group and π-Electron System. *J. Phys. Chem. Lett.* **2019**, *10* (13), 3621−3629.
(35) Li, J.; Shi, J.; Fang, X.; Zhang, Y.; Xie, Q.; Danzeng, Q.; Hu, J.; Zhou, C.-H.; Xia, Z.; Liu, C. Tuning the Excited-State Intramolecular Proton Transfer in Carbon Dots via Coordination with Metal Ion. *Inorg. Chem.* **2025**, *64*, 7706−7715.
(36) Ma, Y.; Zhao, J.; Cheng, L.; Li, C.; Yan, X.; Deng, Z.; Zhang, Y.; Liang, J.; Liu, C.; Zhang, M. Versatile carbon dots with superoxide dismutase-like nanozyme activity and red fluorescence for inflammatory bowel disease therapeutics. *Carbon* **2023**, *204*, 526−537.
(37) Pan, L.; Sun, S.; Zhang, L.; Jiang, K.; Lin, H. Near-infrared emissive carbon dots for two-photon fluorescence bioimaging. *Nanoscale* **2016**, *8* (39), 17350−17356.
(38) Boukhvalov, D. W.; Osipov, V. Y.; Murzalinov, D.; Serikkanov, A.; Bi, H. A comprehensive model of carbon nanodots with 0.21nm lattice fringes patterns. *Carbon* **2024**, *225*, No. 119101.
(39) Zhang, J.; Lu, X.; Tang, D.; Wu, S.; Hou, X.; Liu, J.; Wu, P. Phosphorescent Carbon Dots for Highly Efficient Oxygen Photosensitization and as Photo-Oxidative Nanozymes. *ACS Appl. Mater. Interfaces* **2018**, *10* (47), 40808−40814.
(40) Gao, W.; He, J.; Chen, L.; Meng, X.; Ma, Y.; Cheng, L.; Tu, K.; Gao, X.; Zhang, M.; Yan, X.; Liu, C.; Fan, K.; Pang, D.-W. Deciphering the catalytic mechanism of superoxide dismutase activity of carbon dot nanozyme. *Nat. Commun.* **2023**, *14* (1), No. 160.
(41) Zhang, Y.; Gao, W.; Ma, Y.; Cheng, L.; Zhang, L.; Liu, Q.; Chen, J.; Zhao, Y.; Tu, K.; zhang, M.; Liu, C. Integrating Pt nanoparticles with carbon nanodots to achieve robust cascade superoxide dismutase-catalase nanozyme for antioxidant therapy. *Nano Today* **2023**, *49*, No. 101768.
(42) Kim, H.; Lee, Y. R.; Jeong, H.; Lee, J.; Wu, X.; Li, H.; Yoon, J. Photodynamic and photothermal therapies for bacterial infection treatment. *Smart Mol.* **2023**, *1* (1), No. e20220010.
(43) Osborn, M. J.; Rothfield, L. Cell shape determination in *Escherichia coli*. *Curr. Opin. Microbiol.* **2007**, *10* (6), 606−610.
(44) Saraiva, B. M.; Sorg, M.; Pereira, A. R.; Ferreira, M. J.; Caulat, L. C.; Reichmann, N. T.; Pinho, M. G. Reassessment of the distinctive geometry of Staphylococcus aureus cell division. *Nat. Commun.* **2020**, *11* (1), No. 4097.
(45) Wu, J.; Wang, W.; Shen, J.; Zhou, N.; Li, Y.; Tang, B. Z.; Zhang, M. A Thermosensitive Hydrogel with Efficient NIR Photothermal Conversion as Injectable Wound Dressing for Accelerating Skin Wound Healing. *Adv. Funct. Mater.* **2024**, *34*, No. 2312374.
(46) Liang, M.; Wang, Y.; Ma, K.; Yu, S.; Chen, Y.; Deng, Z.; Liu, Y.; Wang, F. Engineering Inorganic Nanoflares with Elaborate Enzymatic Specificity and Efficiency for Versatile Biofilm Eradication. *Small* **2020**, *16* (41), No. 2002348.
(47) Guo, H.; Luo, H.; Ou, J.; Zheng, J.; Huang, C.; Liu, F.; Ou, S. Preparation of a chitosan/polyvinyl alcohol-based dual-network hydrogel for use as a potential wound-healing material for the sustainable release of drugs. *Carbohydr. Polym.* **2025**, *348*, No. 122822.
(48) Kumar, A.; Han, S. S. PVA-based hydrogels for tissue engineering: A review. *Int. J. Polym. Mater. Polym. Biomater.* **2017**, *66* (4), 159−182.
(49) Zhong, Y.; Lin, Q.; Yu, H.; Shao, L.; Cui, X.; Pang, Q.; Zhu, Y.; Hou, R. Construction methods and biomedical applications of PVA-based hydrogels. *Front. Chem.* **2024**, *12*, No. 1376799.
(50) Liang, Y.; He, J.; Guo, B. Functional Hydrogels as Wound Dressing to Enhance Wound Healing. *ACS Nano* **2021**, *15* (8), 12687−12722.

https://doi.org/10.1021/acsami.5c05025
ACS Appl. Mater. Interfaces 2025, 17, 26467−26479